

Effective transport properties of the porous electrodes in solid oxide fuel cells

H-W Choi¹, A Berson¹, J G Pharoah^{1*}, and S B Beale²

¹Queen's-RMC Fuel Cell Research Centre, Queen's Kingston, Kingston, ON, Canada

²National Research Council, Ottawa, ON, Canada

The manuscript was received on 15 June 2010 and was accepted after revision for publication on 19 October 2010.

DOI: 10.1177/2041296710394266

Abstract: This article presents a numerical framework for the computation of the effective transport properties of solid oxide fuel cells (SOFCs) porous electrodes from three-dimensional (3D) constructions of the microstructure. Realistic models of the 3D microstructure of porous electrodes are first constructed from measured parameters such as porosity and particle size distribution. Then each phase in the model geometries is tessellated with a computational grid. Three different types of grids are considered: Cartesian, octree, and body-fitted/cut-cell with successive levels of surface refinement. Finally, a finite volume method is used to compute the effective transport properties in the three phases (pore, electron, and ion) of the electrode. To validate the numerical approach, results obtained with the finite volume method are compared to those calculated with a random walk simulation for the case of a body-centred cubic lattice of spheres. Then, the influence of the sample size is investigated for random geometries with monosized particle distributions. Finally, effective transport properties are calculated for model geometries with polydisperse particle size distributions similar to those observed in actual SOFC electrodes.

Keywords: effective transport property, solid oxide fuel cells, porous electrodes, finite volume method, random walk simulation

1 INTRODUCTION

The porous composite anode and cathode electrodes used in solid oxide fuel cells (SOFCs) provide a particular challenge to the engineer who wishes to construct mathematical models at the cell/stack level [1, 2]. It is of great importance, not only to employ well-constructed microstructures, but also to possess accurate data for effective transport and electro-physical properties of the multi-phase porous systems used in SOFCs. Properties evaluated from such microscale calculations can then be directly employed to perform computations on a continuum level. In addition, parametric studies can be used to optimize porous microstructures (size, shape, distribution, percolation network, etc.) and hence improve the overall performance of the fuel cell. Therefore, this article focuses on

the computational techniques used to evaluate effective transport and physical properties for the porous and composite electrode materials used in SOFCs.

It is recognized that the porous materials used in SOFC electrodes and their microstructures affect the cell performance by influencing the transfer rates [3, 4]. Features such as the particle size distributions, composition, porosity, and percolation network can influence parameters such as the total and active triple-phase boundary length, the gas-solid internal surface area, the pore size distribution, and transport coefficients. Typically, modelling techniques have employed closure assumptions based on local volume-averaged properties and additionally assumed that the electrodes are homogeneous, relying on semi-empirical correlations [5–10] to describe the transport of gas and charged species through the porous electrodes. SOFC electrodes have a wide variety of pore sizes and contain highly tortuous networks of solid/pore phases, and the microstructure features may be incorrectly described by some correlations. Experimental techniques [11–14] have been used

*Corresponding author: Queen's-RMC Fuel Cell Research Centre, 945 Princess Street, 2nd Floor, Kingston, ON, K7L 5L9, Canada.
email: pharoah@me.queensu.ca

to measure effective conductivities and diffusivities; however, performing direct measurements on each sample material, for all possible phase properties and volume fractions, is prohibitive from a time and cost standpoint.

It is important to utilize well-constructed microstructures for random porous anode and cathode electrodes used in SOFCs. The construction of porous heterogeneous media can be based on a mathematical model or statistical correlation [15–22]. Another useful methodology is the reconstruction of a three-dimensional (3D) geometry using information obtained from a series of two-dimensional (2D) micrograph images of the microstructure followed by data image processing approaches [23–31]. The medium can, for example, be a random packing of spheres [32–36], a dispersion of particles [37], or a digitized image [17, 25, 38, 39]. Among the numerous approaches to reconstruct random media, the present authors follow the reconstruction work of reference [40]. In the present work, the medium is represented by a dispersion of spherical particles randomly dropped into a domain of specified dimensions. The particles are allowed to roll over others until they either contact three others or touch the bottom of the domain.

The study of the effective transport properties has long been an interesting and challenging problem and it manifests technological importance in heterogeneous materials [41]. The effective properties of the heterogeneous material are determined by averages of local fields derived from the underlying governing equations. Specifically, the effective property is defined by a linear constitutive relation between an average of a generalized local flux and an average of a generalized local (or applied) intensity such as temperature gradient, concentration gradient, electric field, magnetic field, etc. [42]. There are a number of approaches to investigate effective physical properties in the literature [5–10, 24, 31, 43–50]. Among theoretical approaches, Maxwell [9] approximated an expression for the effective conductivity of a dilute dispersion of spheres. In contrast to Maxwell's approach, Bruggeman [6] and Landauer [8] approximated the effective conductivities by solving implicit equations for the effective properties. Archie [5] reproduced an empirical law by further modifying Bruggeman's differential effective-medium estimate [6]. Archie's power law [5], frequently applied to porous media as used in fuel cell applications, is given as follows

$$\frac{\alpha^{\text{eff}}}{\alpha} = \epsilon^n \quad (1)$$

where ϵ is the volume (or bond) fraction of a given phase and n is an exponent ($1.5 \leq n \leq 4$). On the other hand, percolation theory [7, 10], applied to estimate the effective properties for binary and multi-component mixtures of particles, obeys the scaling law

such that

$$\alpha^{\text{eff}}(\epsilon) \sim (\epsilon - \epsilon_c)^n \quad (2)$$

where ϵ_c refers to the percolation threshold. Direct measurements of microstructures and subsequent evaluation of effective properties using focused ion beam-scanning electron microscopy (FIB-SEM) [23, 24, 51] and X-ray computed microtomography (XCT) [52, 53] have been published. However, the measurement techniques require large amounts of high-resolution data for image and statistical processing. This is inevitably very expensive in terms of computational resources. To overcome the computational cost issues, various numerical techniques have been applied on the reconstructed geometries. Random walk (RW) calculations [24, 43–46, 48–50], based on simulating the Brownian motion of a diffusing particle [54], have been extensively used to evaluate the effective diffusivity in the pore phase (fluid). Alternatively, continuum-based methods [20, 22, 24, 31, 47, 55, 56] were used to evaluate effective transport properties by solving Laplace equations.

This article presents a numerical procedure for the computation of the effective transport properties in porous SOFC electrodes based on microscopic constructions of the geometry. The proposed computational technique differs from previous approaches in a number of ways. First, the porous microstructure is numerically reconstructed by using measured parameters [14, 24, 26, 28–31, 40, 51] (i.e. values match the properties of real electrodes). The measurable parameters such as the particle size distributions of ceramic powders, the solid volume fraction of lanthanum strontium manganite (LSM) and yttria-stabilized zirconia (YSZ) phases, and the porosity are used as the input parameters to reconstruct the microstructure. Second, three different types of computational grids are considered: Cartesian, non-conforming octree [57, 58], and unstructured body-fitted/cut-cell [59–61]. In each case, the grid passes through all three distinct phases (pore, electron, and ion). Note that the grid generation rationale may readily be applied to any imported type of data such as surface computer-aided design (CAD) geometries or volumetric pixel (voxel) maps as inputs. This technique can therefore accommodate surface or volumetric imaging data from FIB-SEM and XCT [23, 24, 26–31, 51–53]. Finally, both the finite volume method (FVM) and the RW method are used to perform calculations of effective transport coefficients of the pore, electron, and ion phases. The FVM code used in this study is MICROFOAM, which is a suitably modified version of the open-source computational fluid dynamics (CFD) code OpenFOAM® [62]. The effective transport properties can be exploited in cell-level models of SOFCs to simulate transport in the porous electrodes [63–69]. In addition, the computational grids developed in this work along with the

associated reconstructed microstructures can also be used to perform detailed microscopic simulations of SOFCs [3, 20, 70].

The article is organized as follows. Section 2 briefly describes the geometric construction procedure. In section 3, the numerical methodology, as used in this study, is introduced. Section 4 presents validation of the technique, and also the results of parametric studies on the influence of the microstructure characteristics on effective transport properties. Finally, a

summary of results and general conclusion are given in section 5.

2 SAMPLE STRUCTURE RECONSTRUCTION

2.1 Three-dimensional porous structure generation

Porous micro/nano-structures are loose random packings of different types of spherical particles. The

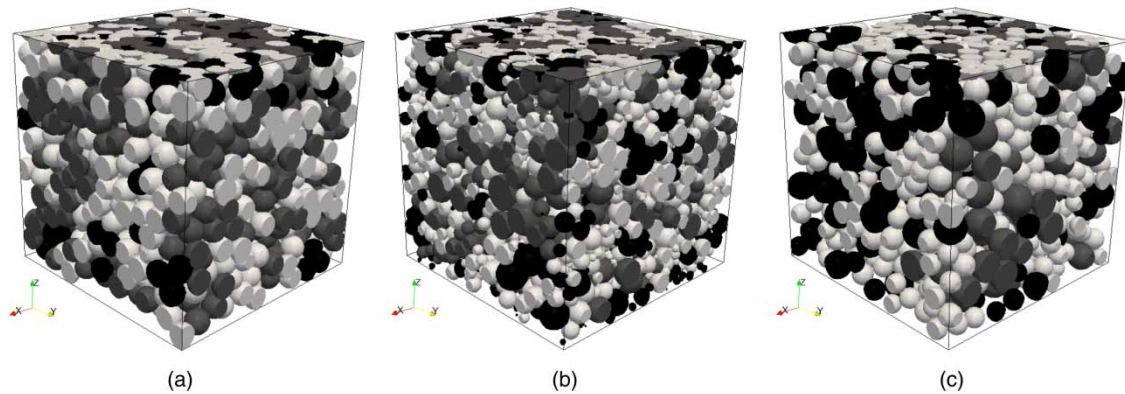


Fig. 1 Microstructure samples consisting of randomly placed spheres: (a) a monosized case with $d = 1 \mu\text{m}$ and $\epsilon = 0.3$; (b) a polydisperse case for the cathode with $d_{\text{elec}} = 0.732 \mu\text{m}$ ($\sigma = 0.284 \mu\text{m}$), $d_{\text{ion}} = 0.51 \mu\text{m}$ ($\sigma = 0.242 \mu\text{m}$) and $\epsilon = 0.35$; and (c) a polydisperse case for the anode with $d_{\text{elec}} = 1.401 \mu\text{m}$ ($\sigma = 0.07 \mu\text{m}$), $d_{\text{ion}} = 0.96 \mu\text{m}$ ($\sigma = 0.065 \mu\text{m}$) and $\epsilon = 0.44$, where d_{elec} is the electron phase particle mean diameter, d_{ion} is the ion phase particle mean diameter, and σ denotes the standard deviation. Dark-grey-coloured particles are 'electron' phase whereas light-grey-coloured particles are 'ion' phase. Non-percolating (i.e. unconnected or isolated) particles are coloured in black. They do not contribute to the solution. Sample sizes of microstructures are cubic domain sizes of 10^3 , 10^3 , and $20^3 \mu\text{m}^3$, respectively

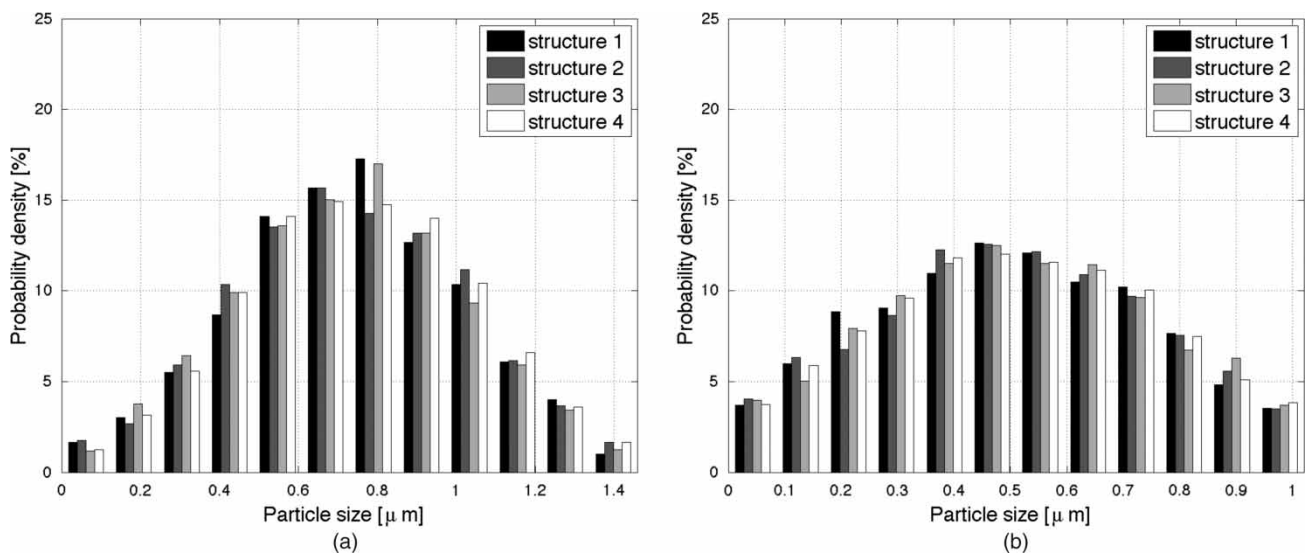


Fig. 2 Sample particle size distributions in the case of polydisperse cathodes for $d_{\text{elec}} = 0.732 \mu\text{m}$ ($\sigma = 0.284 \mu\text{m}$), $d_{\text{ion}} = 0.51 \mu\text{m}$ ($\sigma = 0.242 \mu\text{m}$) and $\epsilon = 0.35$: (a) electron phase particle size distribution and (b) ion phase particle size distribution. Sample domain size of microstructures is cubic domain size of $10^3 \mu\text{m}^3$. Only four structures are demonstrated out of total 20 reconstructed microstructures

size of each type of particle follows a normal distribution. However, any type of particle size distribution can be implemented. The reconstruction procedure used in this study follows the 'drop-and-roll' algorithm given in reference [40]. A particle is randomly dropped

into a cubic domain of specified dimensions. The particle is allowed to roll over other particles until it touches either three other particles or the bottom of the domain. The desired volume fraction of the electron and ion phases is enforced by assigning a

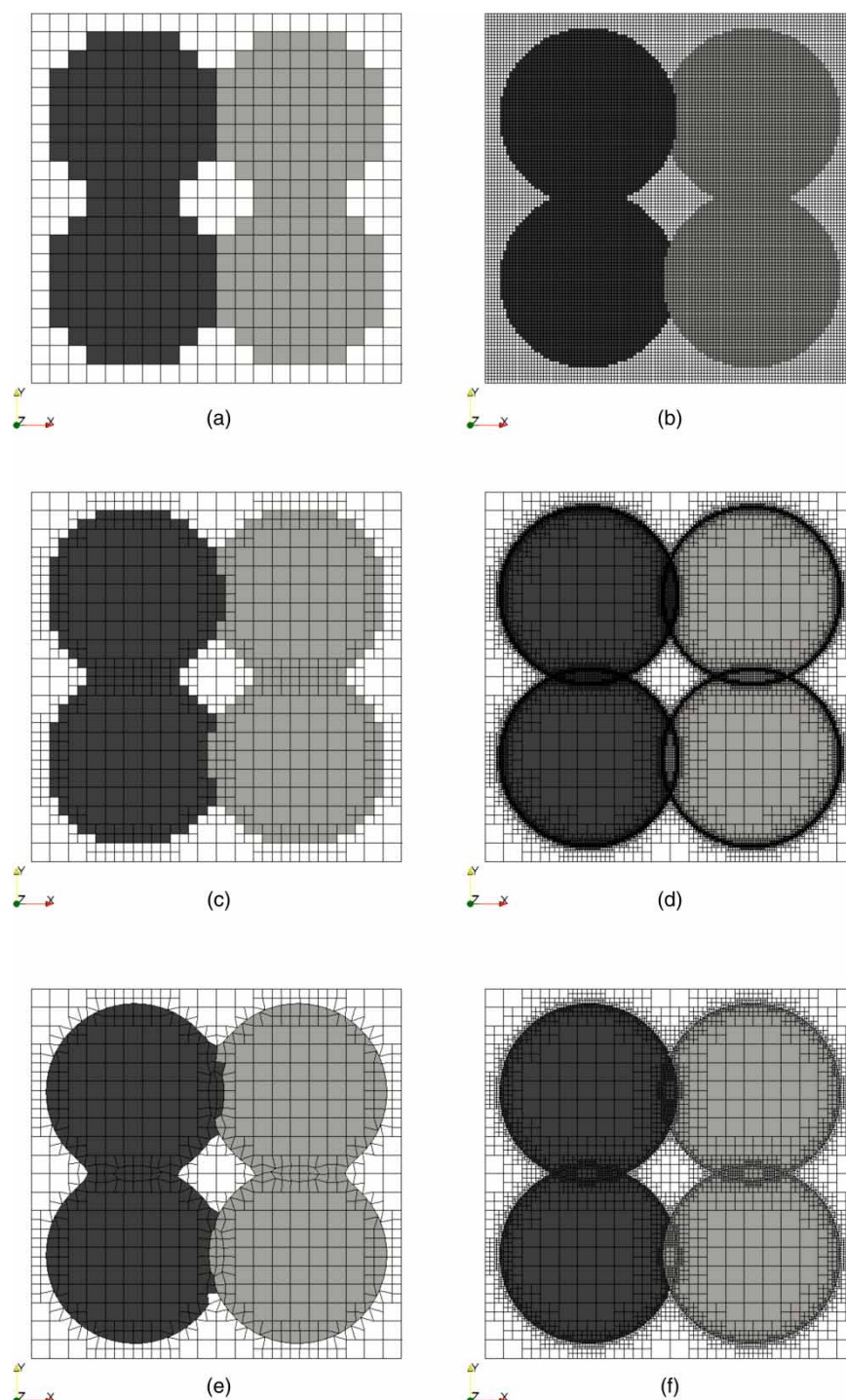


Fig. 3 Examples of the types of computational grids used in this study: (a) 20×20 Cartesian mesh; (b) 120×120 Cartesian mesh; (c) octree mesh after first refinement; (d) after third refinement; (e) body-fitted/cut-cell mesh after first refinement; and (f) after third refinement. Dark grey particles indicate the electron phase whereas light grey particles indicate the ion phase. The white space represents the pore space

weighted probability to the particle selection before the particle is dropped. SOFC electrodes undergo particle sintering during fabrication. To capture this effect, the minimum allowable distance between two contacting particles is varied until the desired porosity (the volume fraction of the pore phase) is obtained. This changes the particle-to-particle contact angle allowing for densification of the structure and simulates various degrees of sintering. The contact angle is a function of the size ratio of the contacting particles and varies throughout the structure. The centre co-ordinates, particle diameter, and the contacting (neighbour) particles are obtained for each particle within the domain.

The transport coefficients of porous electrodes are modified to account for the tortuous pathway of the transported species. To evaluate the effective transport properties of a microstructural sample, a cubic geometry consisting of randomly placed spheres, as shown in Fig. 1, is considered. This geometry is designed to reflect the microstructure of a typical air-sprayed electrode fabricated in the laboratory. The geometry is constructed using three cases: a 'monosized' case where the two ceramic powders have a uniform particle size, a 'polydisperse' case for the cathode where the particle size distributions of LSM and YSZ powders are similar to those in the work of reference [40], and a 'polydisperse' case for the anode where the particle distributions of Ni and YSZ powders are similar to those in the work of reference [51]. Sample particle size distributions are given in Fig. 2, in the case of polydisperse cathodes.

2.2 Grid generation

The geometric properties of the microstructure (e.g. the centre co-ordinates and particle diameters of overlapping spheres) are used as input parameters to construct the computational grids. Three different types of computational grids are considered here.

1. Voxel maps of the three phases (pore, electron and ion) are constructed. The entire region is tessellated into a 3D Cartesian grid, and the electron and ion phases are identified by parsing through the solid (electron and ion) particles. Untagged space is automatically assigned to the pore phase.
2. Using successive h-grid refinement, an octree grid [57, 58] is obtained. The process is reiterated until a satisfactory mesh near the phase interfaces is obtained.
3. Finally, the grid is adapted to the spherical surfaces, and a body-fitted/cut-cell type mesh [59–61] is obtained from the octree grid.

Thus three distinct types of numerical meshes, Cartesian, octree and body-fitted/cut-cell grids, are considered in this study.

Examples of these three mesh types are shown in Fig. 3, displayed in 2D for convenience. The reader will note that unconnected or isolated pores/particles are simply removed from the mesh(es). Examples of these are shown in Fig. 1. It is important to identify these non-percolating regions from the structure as they do not contribute to the solution and may cause divergence while needlessly increasing computational requirements.

3 METHODOLOGY

3.1 Finite volume method

Transport of gas species, ions, and electrons within the three phases of the electrode microstructures is presumed to be dominated by diffusion. For each phase, the governing equation of these diffusive processes can be written as follows

$$\nabla \cdot (\alpha \nabla \phi) = 0, \quad \text{on } \Omega_{\text{phase}} \quad (3)$$

where α is the bulk exchange coefficient, ϕ is the relevant state variable, and Ω_{phase} is the computational domain. Dirichlet boundary conditions are imposed on the top and bottom surfaces, that is, $\phi = \phi_1$ and $\phi = \phi_0$, and symmetry (i.e. zero-flux Neumann) boundary conditions are considered on solid (electron and ion) and pore phase interfaces as well as on the sides of each phase domain, $\partial\phi/\partial n = 0$.

Integrating the diffusion equation (3) over the computational cell and transforming the volume integral of the diffusion into a surface integral through the use of the divergence theorem, the discretized form of the governing equation using the FVM is obtained such that

$$\int_{\Omega} \nabla \cdot (\alpha \nabla \phi) d\Omega = \oint_{\partial\Omega} (\alpha \nabla \phi) \cdot \mathbf{n} dS = 0, \quad \Omega \in \Omega_{\text{phase}} \quad (4)$$

$$\sum_{\text{face}} \mathbf{S}_f \cdot (\alpha \nabla \phi)_f = 0 \quad (5)$$

where Ω_{phase} denotes the phase domain, \mathbf{n} indicates the unit outward-facing normal vector on the boundary surface $\partial\Omega$, \mathbf{S}_f is the outward-pointing face area vector, and subscript f denotes the 'face' of the control volume. The above system is independently solved by the FVM for each phase (i.e. pore, electron, or ion) on the discretized computational grid using MICROFOAM, based on the open-source CFD toolkit OpenFOAM (open field operation and manipulation) [62, 71]. OpenFOAM is based on a flexible set of efficient modules and is able to facilitate complex multi-physics applications. Meshes from a variety of sources and surface geometries from stereolithography CAD formats can be imported, converted, and manipulated.

The code structure is kept 'open' so users can extend and create their own solvers, libraries, and toolboxes. It is written in the object-oriented C++ programming language. Recently, OpenFOAM has been applied to some fuel cell applications [72–74].

The linear algebraic equations may be expressed as a sparse matrix, which has a complex structure requiring indirect addressing and appropriate solvers. Hence, equation (5) expressed over the entire computational domain yields a system in the matrix form of

$$\mathbf{A}\Phi = \mathbf{f} \quad (6)$$

where the matrix \mathbf{A} is a sparse matrix that can be inverted iteratively, \mathbf{f} is a forcing vector and Φ is a solution field of linear system. OpenFOAM currently uses the conjugate-gradient method, with incomplete Cholesky preconditioning to solve a symmetric matrix such as equation (6).

From the solution of equation (6), the effective transport coefficient for gas diffusion ($\alpha^{\text{eff}} = D^{\text{eff}}$), the effective electronic conductivity ($\alpha^{\text{eff}} = \kappa_{\text{elec}}^{\text{eff}}$), and the effective ionic conductivity ($\alpha^{\text{eff}} = \kappa_{\text{ion}}^{\text{eff}}$) can be obtained. The calculation procedure for the effective coefficients can be found in references [47] and [56]. The local flux can be related to the generalized local concentration gradient such that

$$\mathbf{q} = -\alpha \nabla \phi \quad (7)$$

where \mathbf{q} is derived from the calculated solution (ϕ) of equation (3). The average (surface-integrated) local flux across the boundary surface of each phase is given as

$$\int_{\partial\Omega} \mathbf{q} \, dS = \int_{\partial\Omega_{\text{phase}}} -\alpha \frac{\partial \phi}{\partial n} \, dS \quad (8)$$

and hence the effective transport coefficients can be calculated by substituting equation (7) into equation (8) such that

$$\alpha^{\text{eff}} = \frac{\int_{\partial\Omega_{\text{phase}}} \alpha (\partial \phi / \partial n) \, dS}{(\Delta \phi / L) S} \quad (9)$$

where $\Delta \phi$ represents the potential difference, L is the selected length of the computational domain, and S denotes the selected boundary surface area of each phase.

3.2 RW simulation: mean-square displacement method

The results obtained with the MICROFOAM solver are compared with an RW simulation for validation. Among a number of RW simulation approaches [24, 33, 43–45, 48–50, 75–77], this article follows the algorithm proposed by Berson *et al.* [78]. In the RW

simulation, the effective diffusion coefficient of a given phase is computed using the mean-square displacement method. It relies on the basic principles of Brownian motion, as formulated by Einstein [54] (i.e. the irregular molecular movement of gas particles results in a diffusion process). The diffusion coefficient of the gas, α , is related to the mean-square displacement ($\langle \xi^2 \rangle$) of a large number of gas particles. Therefore, in three dimensions, assuming the particles are spherical

$$\alpha = \frac{\langle \xi^2 \rangle}{6t} \quad (10)$$

where t is the travel time.

In practice, a particle is randomly positioned in the phase domain and allowed to travel randomly during a prescribed amount of time t or until it has traveled a prescribed distance s . Then the displacement ξ between the original location of the particle and its final location is measured. The process is repeated for a large number of particles and the diffusion coefficient is computed from equation (10). Particles collide with each other as well as with the phase interface (diffuse reflection at the wall). In this work, only the effect of the geometry on effective transport properties is considered (i.e. the number of inter-particle collisions is much larger than the number of collisions with interfaces). This is achieved by ensuring that the mean free path (i.e. the mean distance between inter-particle collisions) is presumed to be much smaller than the characteristic length of the considered phase. In other words, only the bulk diffusion regime is considered. The issue of the diffusion regime for the gas phase in SOFC is addressed in reference [78]. Note that RW simulations are performed in analytical geometries (i.e. continuous geometries for which spherical particles are described by analytical expressions). For the domain size used in this study, boundary conditions do not have a significant impact on the solution, so symmetry boundary conditions are used in agreement with the MICROFOAM calculations.

4 NUMERICAL RESULTS

Effective properties calculated by the numerical techniques are given below. The microstructures considered in this article are described in Table 1. The first case considered is an idealized porous medium, namely, a periodic array of a body-centred cubic (BCC) lattice of spheres as shown in Fig. 4. For this case, the FVM data obtained with MICROFOAM are compared against RW simulations to demonstrate grid independence. Subsequently, a domain size study allows for the determination of the minimum sample domain size: since the domain size influences the results as well, it is important to identify a minimum sample domain size. The domain size study is performed on random porous structures with monosized particles

Table 1 Description of reconstructed microstructures considered in this study

Case	Type	Mean diameter		Sample domain
1	BCC	d	0.434	$1 \times 1 \times 1$
2a	Monosized	d (μm)	1	$5 \times 5 \times 5$
2b			1	$10 \times 10 \times 10$
2c			1	$15 \times 15 \times 15$
3	Polydisperse (cathode)	$d_{\text{elec}} \pm \sigma$ (μm)	$d_{\text{ion}} \pm \sigma$ (μm)	$10 \times 10 \times 10$
4a	Polydisperse (anode)	$d_{\text{elec}} \pm \sigma$ (μm)	$d_{\text{ion}} \pm \sigma$ (μm)	$20 \times 20 \times 20$
4b		1.401 ± 0.070	0.960 ± 0.065	
4c		1.516 ± 0.082	1.179 ± 0.116	
4d		2.219 ± 0.145	1.207 ± 0.077	
4e		2.132 ± 0.165	1.288 ± 0.149	
4f		1.902 ± 0.078	1.478 ± 0.154	
		2.707 ± 0.328	1.681 ± 0.149	

BCC denotes the body-centred cubic lattice of spheres

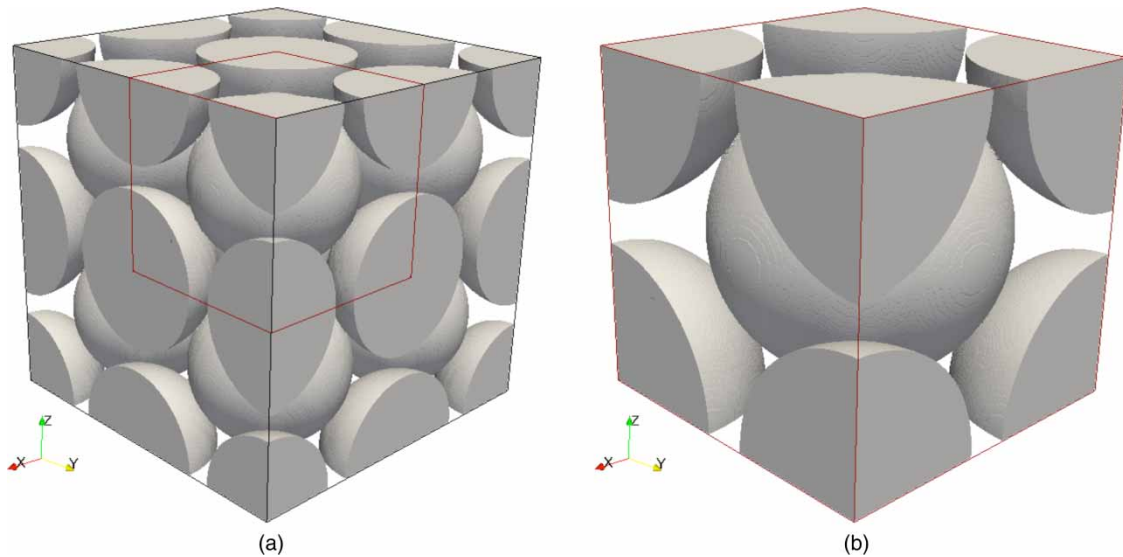


Fig. 4 BCC lattice of spheres in a cubic domain: (a) configuration for 35 packing spheres and (b) configuration for nine packing spheres. Note that configuration (b) is the representative configuration of configuration (a) or larger configurations.

for three different cases. Finally, the effect of the level of grid surface refinement (octree, cut-cell, etc.) on the results is investigated for random porous media with polydisperse particle size distributions available in the literature [40, 51].

4.1 BCC lattice of spheres

In order to validate the methodology, an array of spheres is considered, namely a BCC lattice of spherical particles with equal radii of 0.434. For this case the particles overlap a little (the radial overlap is 0.002), in order to ensure that both solid and pore phases are connected from one end to the other, in a continuous manner. The solid and pore phases are considered separately when calculating the effective transport

Table 2 RW simulation results for analytical domain of the BCC lattice of spheres with $N_{\text{sample}} = 10,005,500$ where $\sigma/\sqrt{N_{\text{sample}}}$ denotes the estimated error for the RW simulation

N_{sample}	D^{eff}/D	$\sigma/\sqrt{N_{\text{sample}}}$
10,005,500	0.21395	5.8725×10^{-5}

properties (although this would not necessarily be true when considering, say, effective thermal conductivity). To compare numerical results calculated by MICROFOAM, an RW simulation is also considered. Over 10 million random particles are used to sample RW calculations. Note that based on the central limit theorem [79], the estimated error of the RW algorithm

decreases as a function of $1/\sqrt{N_{\text{sample}}}$ and eventually converges to 0 for a 'large enough' number of samples, that is, $N_{\text{sample}} \rightarrow \infty$. Continuum RW simulation is considered here only for the 'pore' phase of the BCC lattice of spheres. The RW algorithm for analytical geometries will be extended to solve the electronic and ionic phases in the future. RW simulation results for analytical domain of the BCC lattice of spheres are summarized in Table 2. With over 10 million random particles, the estimated error of the RW simulation, $\sigma/\sqrt{N_{\text{sample}}}$, is as small as 0.005 87 per cent. Therefore, the solution from the RW simulation for the analytical domain given in Table 2 is used as a reference solution for the pore phase of the BCC lattice of spheres. In this study, FVM is used on three different computational grids as shown in Fig. 5, whereas RW simulation is applied to the Cartesian grid and the analytical domain. A comparison of the two numerical models

is shown in Fig. 6 for the pore phase domain of the BCC lattice. It can be seen that the FVM results on the body-fitted/cut-cell mesh and the reference solution are in excellent agreement for all quantities, porosity and gas diffusivity. In addition, solutions from the FVM on the body-fitted/cut-cell mesh exhibit much faster convergence to the correct solution than the calculations performed with the other computational grids. Although both FVM and RW on the Cartesian mesh provide the slowest grid (spatial) convergence, the two different methods are nonetheless in fairly good agreement. Nevertheless, use of the Cartesian grids for both FVM and RW require significantly more computational resources than the FVM performed on both the octree and the body-fitted/cut-cell meshes. Figure 6(c) shows a comparison of the proposed numerical models for the solid phase domain of the BCC lattice. Again, the FVM performed on either the octree or the

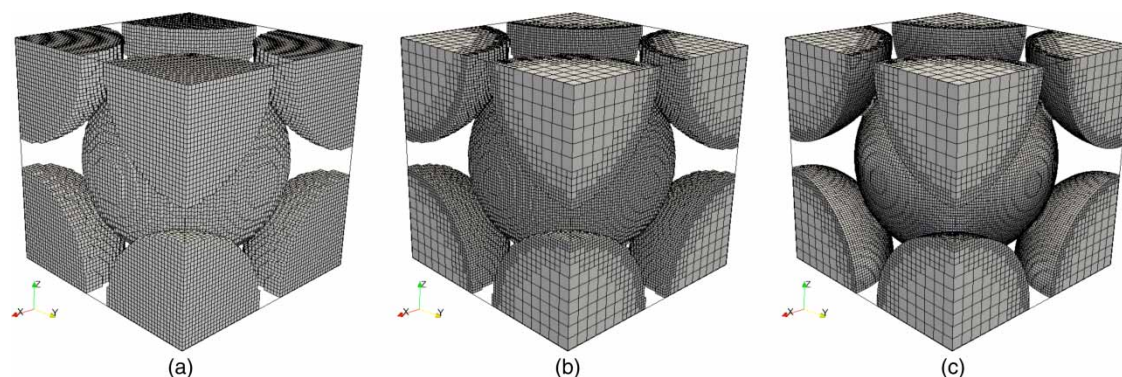


Fig. 5 Computational grids for the BCC lattice of spheres a cube domain: (a) Cartesian grid with 216 000 cells; (b) octree grid with 215 578 cells; and (c) body-fitted/cut-cell grid with 215 578 cells

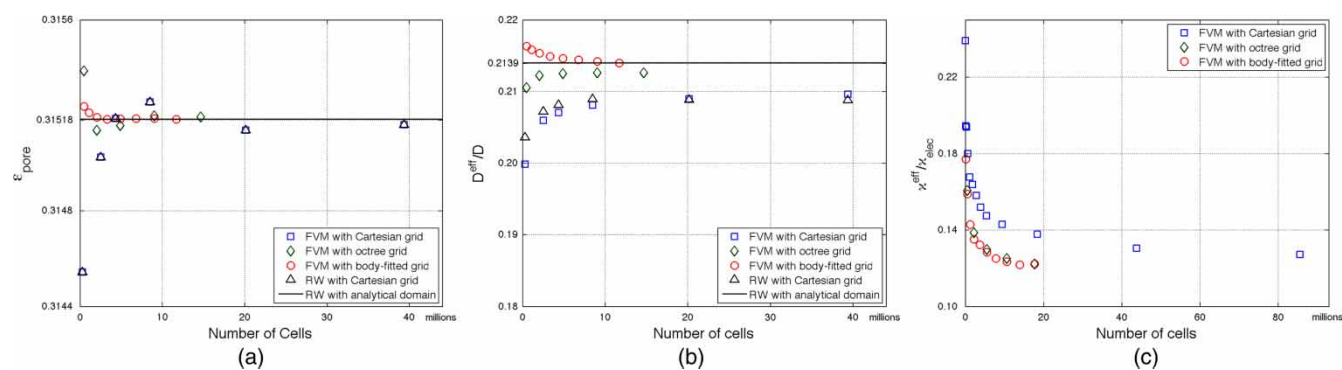


Fig. 6 Comparison of the proposed numerical models for the BCC lattice of spheres: (a) volume fraction of the pore domain (i.e. porosity of the BCC lattice); (b) effective gas diffusivity of the pore phase; and (c) effective conductivity of the solid phase. The porosity of the BCC lattice of spheres is exactly calculated as $\epsilon_{\text{pore}} = 0.3158$ when radii have the value of $r = 0.434$ based on reference [80]. Note that RW simulation for the analytical domain has been developed only for the pore phase domain [78]. The number of cells for the grid resolution used here-in represents the resolution of Cartesian grid used in the grid-based RW simulation (i.e. RW simulation with Cartesian grid). For each Cartesian grid, the RW simulation uses the fixed number of randomly generated particles for sampling (i.e. $N_{\text{sample}} = 100\,000$)

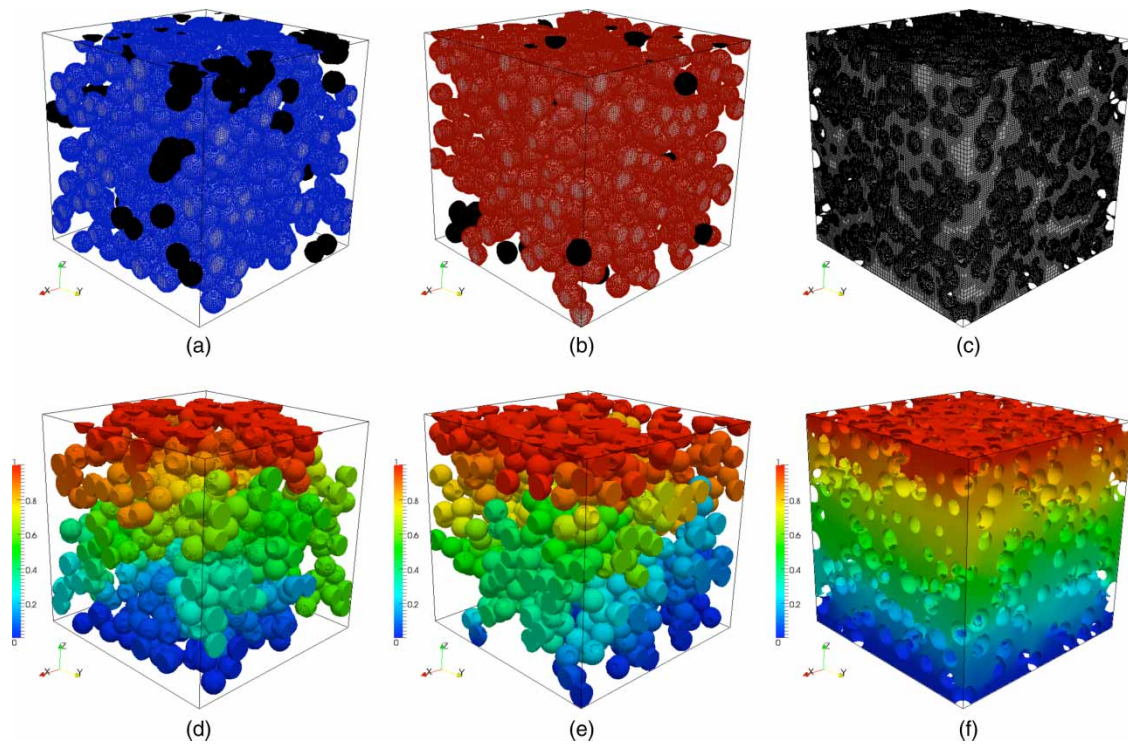


Fig. 7 Monosized particles in a sample domain of $(10 \mu\text{m})^3$: (a) body-fitted grid for electron phase; (b) ion phase; (c) pore phase; (d) FVM solution for electron phase; (e) ion phase; and (f) pore phase. Note that the isolated particles, coloured in black in (a) and (b), were excluded from the calculations

body-fitted/cut-cell meshes provides faster convergence than on the Cartesian grid. It is clearly evident from Fig. 6 that the octree and body-fitted/cut-cell grids are more suitable, for the types of calculation performed in this study, than simple Cartesian grids.

4.2 Sample domain size

Three types of sample structures with monosized particles of diameter $1 \mu\text{m}$ are considered. Domain sizes of $5 \mu\text{m} \times 5 \mu\text{m} \times 5 \mu\text{m}$ ($5^3 \mu\text{m}^3$), $10 \mu\text{m} \times 10 \mu\text{m} \times 10 \mu\text{m}$ ($10^3 \mu\text{m}^3$), and $15 \mu\text{m} \times 15 \mu\text{m} \times 15 \mu\text{m}$ ($15^3 \mu\text{m}^3$) are considered. The sample size of microstructures, the solid phase volume composition, porosity, and the randomness of the structures all influence the calculated results. It is clear that the larger the sample structure size (i.e. structures that contain more particles in the domain) the more computational cost. Therefore, the main motivation for a domain size study is to determine the minimum requirement. An example is displayed in Fig. 7 for a monosized particle distribution of domain size $10^3 \mu\text{m}^3$. Figure 8 displays the electronic and ionic conductivities for monosized particles for three sample structures. A total of 20 structures (the number suggested by Kenney *et al.* [40]) for each sample electrode are constructed for analysing mean values and standard deviations of effective conductivities. For each case, the average porosity ranged from 0.35 to 0.37. The total solid

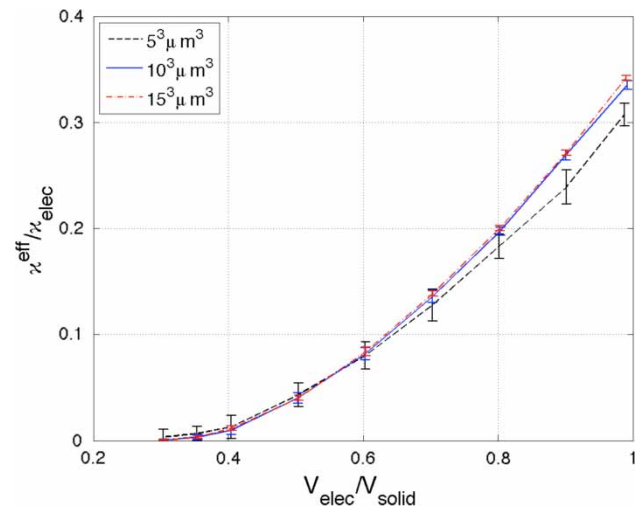


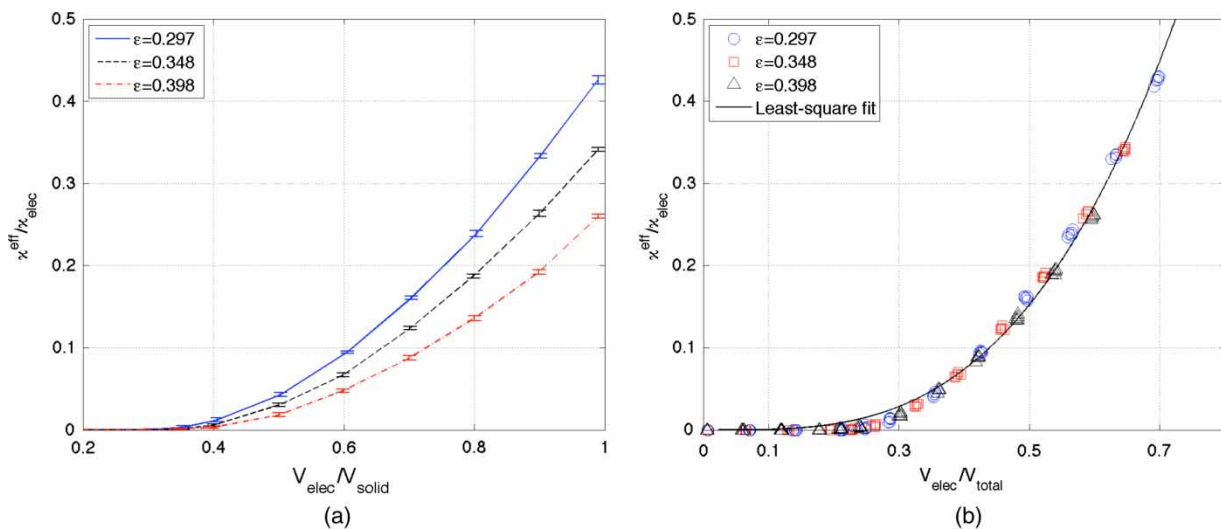
Fig. 8 Electrical conductivities for monosized particles for three sample structures with $\epsilon = 0.356$. Sample domain sizes of 5^3 , 10^3 , and $15^3 \mu\text{m}^3$ are used. The grid resolutions for the sample domain size of 5^3 , 10^3 , and $15^3 \mu\text{m}^3$ are 2 258 787, 3 222 572 and 3 781 791 cells of the body-fitted grids, respectively. The number of cells given here is average values of total 20 reconstructed microstructures

volume fractions range from 0.3 to 0.99. The lower bound on the solid volume fraction is dictated by the threshold below which the structure is not consolidated and conduction no longer occurs. This occurs

Table 3 The electronic or ionic phase volume fractions (out of total solids content), mean and standard deviation (stdev), and estimated error (err) for the monosized particle for three sample structures using the body-fitted grids

5 $\mu\text{m} \times 5 \mu\text{m} \times 5 \mu\text{m}$			10 $\mu\text{m} \times 10 \mu\text{m} \times 10 \mu\text{m}$			15 $\mu\text{m} \times 15 \mu\text{m} \times 15 \mu\text{m}$		
$V_{\text{elec}}/V_{\text{solid}}$	$(\kappa^{\text{eff}}/\kappa) \pm \sigma$	$\sigma/\sqrt{20}$	$V_{\text{elec}}/V_{\text{solid}}$	$(\kappa^{\text{eff}}/\kappa) \pm \sigma$	$\sigma/\sqrt{20}$	$(V_{\text{elec}}/V_{\text{solid}})$	$(\kappa^{\text{eff}}/\kappa) \pm \sigma$	$\sigma/\sqrt{20}$
0.30	0.003 29 \pm 0.007 12	0.001 59	0.30	0.000 49 \pm 0.001 03	0.000 23	0.30	0.000 27 \pm 0.000 51	0.000 11
0.35	0.006 75 \pm 0.006 67	0.001 49	0.35	0.003 45 \pm 0.002 39	0.000 53	0.35	0.003 23 \pm 0.001 52	0.000 34
0.40	0.012 84 \pm 0.010 66	0.002 38	0.40	0.009 83 \pm 0.004 29	0.000 96	0.40	0.011 61 \pm 0.002 13	0.000 48
0.50	0.043 25 \pm 0.011 32	0.002 53	0.50	0.040 30 \pm 0.004 87	0.001 09	0.50	0.040 45 \pm 0.002 55	0.000 57
0.60	0.080 26 \pm 0.012 94	0.002 89	0.60	0.081 82 \pm 0.005 78	0.001 29	0.60	0.083 94 \pm 0.003 94	0.000 88
0.70	0.127 65 \pm 0.014 99	0.003 35	0.70	0.135 77 \pm 0.005 58	0.001 25	0.70	0.138 68 \pm 0.002 30	0.000 51
0.80	0.183 10 \pm 0.011 65	0.002 61	0.80	0.197 32 \pm 0.003 74	0.000 84	0.80	0.200 30 \pm 0.002 61	0.000 58
0.90	0.238 84 \pm 0.016 10	0.003 60	0.90	0.268 99 \pm 0.004 78	0.001 07	0.90	0.271 17 \pm 0.002 48	0.000 56
0.99	0.307 16 \pm 0.010 81	0.002 42	0.99	0.335 00 \pm 0.004 29	0.000 96	0.99	0.341 74 \pm 0.002 23	0.000 50

Cubic sample domain sizes of 5^3 , 10^3 , and $15^3 \mu\text{m}^3$ are used, respectively.

**Fig. 9** Effective electronic conductivities for the reconstructed cathode microstructures: (a) effective electronic conductivity as a volume fractions out of solid contents ($V_{\text{elec}}/V_{\text{solid}}$) and (b) effective electronic conductivity as a function of volume fractions out of the total volume ($V_{\text{elec}}/V_{\text{total}}$). Note that only the mean values are displayed

at below somewhere between 0.3 and 0.4 [81]. Both the Cartesian (i.e. voxel map) and body-fitted/cut-cell grids are employed. Mean values are shown as solid lines, while standard deviations (σ) are displayed as error bars as shown in Fig. 8 for the three sample cases (i.e. cubic domain sizes of 5^3 , 10^3 , and $15^3 \mu\text{m}^3$). Table 3 summarizes the mean value with one standard deviation and the estimated error as functions of the electronic or ionic phase solid volume fractions for monosized particles for three cases. Increasing the domain size from 5^3 to $10^3 \mu\text{m}^3$ changes the solutions by at most 14 per cent when the electronic or ionic phase solid volume fractions are greater than 0.4, whereas increasing the domain size from 10^3 to $15^3 \mu\text{m}^3$ changes the transport coefficient ratio $\kappa^{\text{eff}}/\kappa$ by less than 2.6 per cent. Around the minimum solid volume fraction (i.e. $0.3 \leq V_{\text{elec}}/V_{\text{solid}} \leq 0.4$), the transport coefficient ratio $\kappa^{\text{eff}}/\kappa_{\text{ele}}$ exhibits large variations throughout for all cases considered. However,

generally SOFC electrodes possess matrix compositions larger than these limiting cases. Therefore, with the mean particle diameter of $1 \mu\text{m}$ the sample domain size of $10^3 \mu\text{m}^3$ is proposed as the minimum acceptable size for the cases considered here.

4.3 SOFC electrodes applications

Two types of sample microstructures with polydisperse particle size distributions are now considered. These correspond to a cathode microstructure of LSM and YSZ powders [43] and an anode microstructure of Ni and YSZ powders [59]. Earlier work [43, 59] was confined to quantification of the geometric properties of the electrodes. The present study extends previous work in terms of obtaining results for the effective transport properties of the cathode and anode reconstructions.

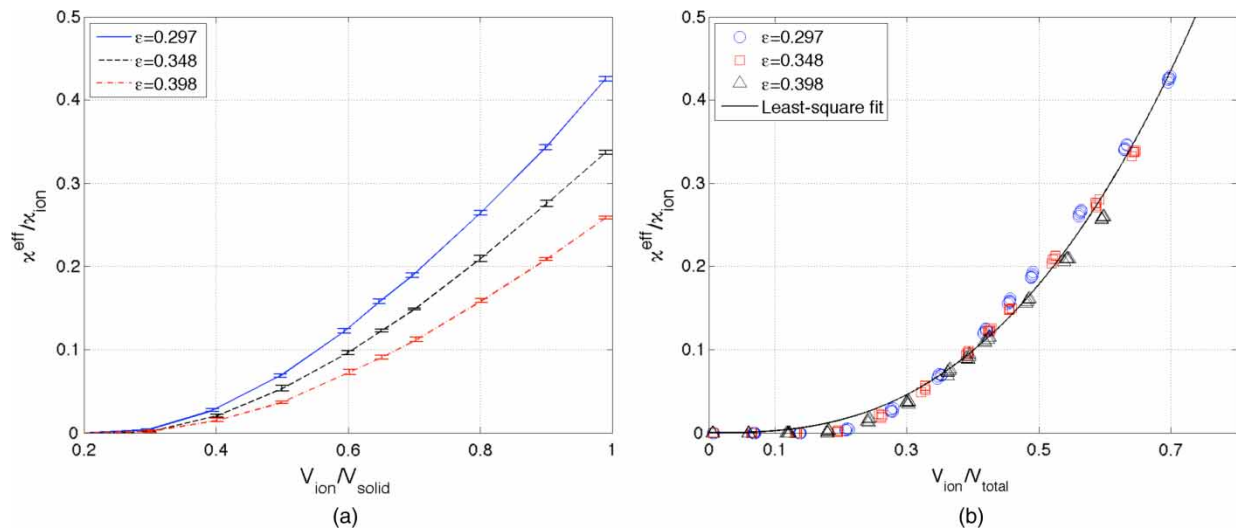


Fig. 10 Effective ionic conductivities for the cathode: (a) ionic conductivity as a function of the ratio of volume fractions of solid contents ($V_{\text{ion}}/V_{\text{solid}}$) and (b) ionic conductivity as a function of the ratio of volume fractions of the total volume ($V_{\text{ion}}/V_{\text{total}}$). Only the mean values are displayed

4.3.1 Cathode construction

To analyse the effects of the morphology of the solid compositions used in the cathode, the solid volume fractions of the electron and ion conducting phases are varied from 0.01 to 0.99 for each one of the following porosity (i.e. $\epsilon = 0.297, 0.348, 0.398$). Figure 9 shows the effective conductivity for the electronically conducting phase. Figure 9(a) shows effective conductivity as a function of the electronic phase solid volume fraction (i.e. $V_{\text{elec}}/V_{\text{solid}}$) in terms of the mean and (one) standard deviation. The effective electronic conductivity increases with decreasing porosity. As is evident from Fig. 9(b), the effective electronic conductivities compress onto a single curve when presented as a function of the electronically conducting phase total volume fraction (i.e. $\epsilon_{\text{elec}} = V_{\text{elec}}/V_{\text{total}}$). Figure 10 presents the effective conductivity for the ionically conducting phase. Figure 10(a) shows that the effective ionic conductivity increases with decreasing porosity. The effective ionic conductivity also collapses onto a single curve when considered to be a function of the ion phase volume fraction (i.e. $\epsilon_{\text{ion}} = V_{\text{ion}}/V_{\text{total}}$) as shown in Fig. 10(b).

4.3.2 Anode construction

Different anode compositions are considered with a solid volume fraction for the electronically conducting phase of 0.47 and the ionically conducting phase of 0.53, and various particle size distributions. The particle size distributions are taken from reference [59] and are summarized in Table 1. The porosity varies from 0.1 to 0.44 between various cases. Figure 11 shows the effective electronic and ionic conductivity as a

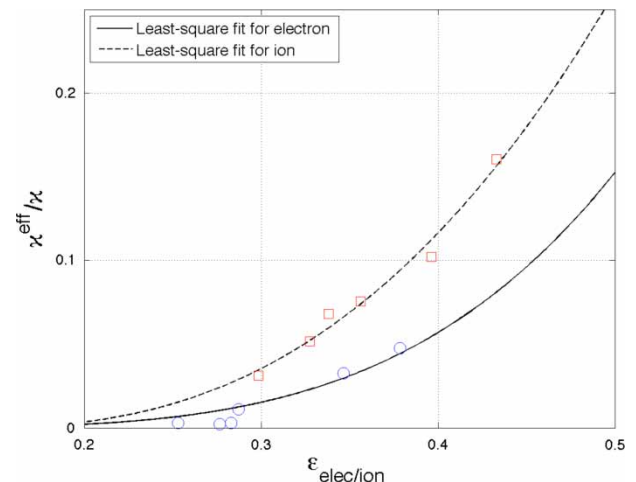


Fig. 11 Effective electronic and ionic conductivity as a function of volume fraction for the anode. Only mean values are displayed

function of the corresponding phase volume fraction. The curve fit of the electronically conducting phase differs from that of the ionically conducting phase. The discrepancy comes from the different particle size distributions between electron and ion phases.

4.3.3 Summary of effective transport properties

This section summarizes effective transport properties evaluated for different types of sample structures, as listed in Table 1. All calculations are performed using the FVM with body-fitted/cut-cell grids. Figures 12(a) and (b) show effective electronic and ionic conductivities for the solid phase and gas diffusivity for the pore phase, respectively. These are to be considered

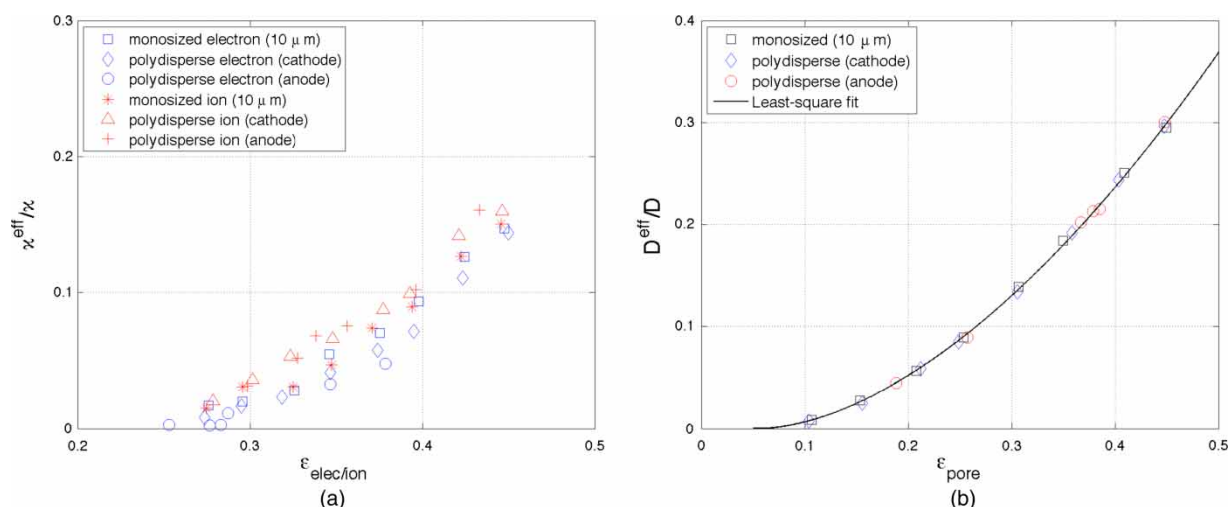


Fig. 12 Effective electronic/ionic conductivity and gas diffusivity: (a) solid (electron and ion) conductivity and (b) gas diffusivity as a function of volume fraction

as a function of the relevant phase volume fractions. Figure 12(b) shows that the effective gas diffusivities for the pore phase can be compressed onto a single curve in terms of the porosity (i.e. $\epsilon = V_{pore}/V_{total}$). However, it is clearly evident from Fig. 12(a) that the same is not true for either electronic or ionic conductivity. Electronic and ionic conductivities depend not only on the volume fraction of the corresponding phase but also on particle size distributions.

5 CONCLUSION

A numerical technique for calculating effective transport properties within porous microstructures was described and detailed. The method was based on the construction of sample structures with morphology similar to those observed in SOFCs. These were used to perform calculations using FVM and RW simulations. Following construction of the 3D random microstructures, the computational meshes were built. Three types of meshes were considered for performing numerical computations: Cartesian, octree, and body-fitted/cut-cell. A periodic array of BCC lattice of spheres was considered to evaluate the scheme from the perspective of grid resolution. It was found that effective transport properties calculated by both FVM using body-fitted/cut-cell grids and the RW simulation using an analytical domain were in excellent agreement. For a sample domain size study, three sample sizes of the reconstructed microstructures, namely domain sizes of 5^3 , 10^3 , and $15^3 \mu m^3$, were considered. It was found that the sample domain size should be at least ten times larger than the mean particle diameter in each direction in order to achieve reliable values for effective transport properties. The proposed technique was applied to

evaluate the effective properties of anodes and cathodes of typical SOFCs. It was observed that single general fitting curve could not be formulated for the effective electronic and ionic conductivities for the cases considered in this study because the values of conductivities were dependent on the particle size distribution. Nevertheless, it was found that the effective gas diffusivities of the pore phase were collapsed onto a single-common curve fit over a wide range of the particle size distributions.

ACKNOWLEDGEMENTS

This research was supported through funding from the NSERC Solid Oxide Fuel Cell Canada Strategic Research Network from the Natural Science and Engineering Research Council (NSERC) and other sponsors listed at www.sofccanada.com. Funding was also provided by the National Research Council of Canada. This work was made possible by the facilities of the Shared Hierarchical Academic Research Computing Network (SHARCNET: www.sharcnet.ca).

© Authors and National Research Council Canada 2011

REFERENCES

- 1 Beale, S. B., Lin, Y., Zhubrin, S. V., and Dong, W. Computer methods for performance prediction in fuel cells. *J. Power Sources*, 2003, **118**(1–2), 79–85.
- 2 Beale, S. B. and Zhubrin, S. V. A distributed resistance analogy for solid oxide fuel cells. *Numer. Heat Trans. B*, 2005, **47**(6), 573–591.
- 3 Abbaspour, A., Nandakumar, K., Luo, J., and Chuang, K. T. A novel approach to study the structure versus

- performance relationship of SOFC electrodes. *J. Power Sources*, 2006, **161**, 965–970.
- 4 Evans, A., Bieberle-Hütter, A., Rupp, J. L. M., and Gaucker, L. J. Review on microfabricated micro-solid oxide fuel cell membranes. *J. Power Sources*, 2009, **194**, 119–129.
 - 5 Archie, G. E. The electrical resistivity log as an aid in determining some reservoir characteristics. *Trans. AIME*, 1942, **146**, 54–61.
 - 6 Bruggeman, D. A. G. Calculation of the various physical constant of heterogeneous substances. I. Dielectric constants and conductivities of mixtures of isotropic substances. *Ann. Phys.*, 1935, **24**, 636–664.
 - 7 Chen, D., Lin, Z., Zhu, H., and Kee, R. J. Percolation theory to predict effective properties of solid oxide fuel-cell composite electrodes. *J. Power Sources*, 2009, **191**, 240–252.
 - 8 Landauer, R. The electrical resistance of binary metallic mixtures. *J. Appl. Phys.*, 1952, **23**, 779–784.
 - 9 Maxwell, J. C. *Treatise on electricity and magnetism*, 1873 (Clarendon Press, Oxford).
 - 10 Staffer, D. *Introduction to percolation theory*, 1985 (Taylor and Francis Ltd, London, UK).
 - 11 Costamagna, P., Panizza, M., Cerisola, G., and Barbucci, A. Effect of composition on the performance of cermet electrodes. Experimental and theoretical approach. *Electrochim. Acta*, 2002, **47**, 1079–1089.
 - 12 Dees, D. W., Claar, T. D., Easler, T. E., Fee, D. C., and Mrazek, F. C. Conductivity of porous Ni/ZrO₂-Y₂O₃ cermets. *J. Electrochem. Soc.*, 1987, **134**, 2141–2146.
 - 13 Lee, J.-H., Moon, H., Lee, H.-W., Kim, J., Kim, J.-D., and Yoon, K.-H. Quantitative analysis of microstructure and its related electrical property of SOFC anode, Ni-YSZ cermet. *Solid State Ionics*, 2002, **148**, 15–26.
 - 14 Yamahara, K., Sholkapper, T. Z., Jacobson, C. P., Visco, S. J., and Jonghe, L. C. D. Ionic conductivity of stabilized zirconia networks in composite SOFC electrodes. *Solid State Ionics*, 2005, **176**, 1359–1364.
 - 15 Gokhale, A. M., Zhang, S., and Liu, M. A stochastic geometry based model for total triple phase boundary length in composite cathodes for solid oxide fuel cells. *J. Power Sources*, 2009, **194**(1), 303–312.
 - 16 Ji, Y., Yuan, K., and Chung, J. N. Monte-Carlo simulation and performance optimization for the cathode microstructure in a solid oxide fuel cell. *J. Power Sources*, 2007, **165**(2), 774–785.
 - 17 Johnson, J. and Qu, J. Effective modulus and coefficient of thermal expansion of Ni-YSZ porous cermets. *J. Power Sources*, 2008, **181**(1), 85–92.
 - 18 Kainourgiakis, M. E., Kikkinides, E. S., and Stubos, A. K. Diffusion and flow in porous domains constructed using process-based and stochastic techniques. *J. Porous Mater.*, 2002, **9**, 141–154.
 - 19 Sundararaghavan, V. and Zabaras, N. Classification and reconstruction of three-dimensional microstructures using support vector machines. *Comput. Mater. Sci.*, 2005, **32**(2), 223–239.
 - 20 Suzue, Y., Shikazono, N., and Kasagi, N. Micro modeling of solid oxide fuel cell anode based on stochastic reconstruction. *J. Power Sources*, 2008, **184**(1), 52–59.
 - 21 Torquato, S. Statistical description of microstructures. *Annu. Rev. Mater. Res.*, 2002, **32**, 77–111.
 - 22 Zhao, X., Yao, J., and Yi, Y. A new stochastic method of reconstructing porous media. *Transp. Porous Media*, 2007, **69**, 1–11.
 - 23 Gostovic, D., Smith, J. R., Kundinger, D. P., Jones, K. S., and Wachsman, E. D. Three-dimensional reconstruction of porous LSCF cathodes. *Electrochem. Solid State Lett.*, 2007, **10**(12), B214–B217.
 - 24 Iwai, H., Shikazono, N., Matsui, T., Teshima, H., Kishimoto, M., Kishida, R., Hayashi, D., Matsuzaki, K., Kanno, D., Saito, M., Muroyama, H., Eguchi, K., Kasagi, N., and Yoshida, H. Quantification of SOFC anode microstructure based on dual beam FIB-SEM technique. *J. Power Sources*, 2010, **195**(4), 955–961.
 - 25 Lanzini, A., Leone, P., and Asinari, P. Microstructural characterization of solid oxide fuel cell electrodes by image analysis technique. *J. Power Sources*, 2009, **194**(1), 408–422.
 - 26 Shearing, P. R., Golbert, J., Chater, R. J., and Brandon, N. P. 3D reconstruction of SOFC anodes using a focused ion beam lift-out technique. *Chem. Eng. Sci.*, 2009, **64**(17), 3928–3933.
 - 27 Smith, J. R., Chen, A., Gostovic, D., Hickey, D., Kundinger, D., Duncan, K. L., DeHoff, R. T., Jones, K. S., and Wachsman, E. D. Evaluation of the relationship between cathode microstructure and electrochemical behavior for SOFCs. *Solid State Ionics*, 2009, **180**(1), 90–98.
 - 28 Wilson, J. R. and Barnett, S. A. Solid oxide fuel cell Ni-YSZ anodes: effect of composition on microstructure and performance. *Electrochem. Solid State Lett.*, 2008, **11**(10), B181–B185.
 - 29 Wilson, J. R., Duong, A. T., Gameiro, M., Chen, H.-Y., Thornton, K., Mummb, D. R., and Barnett, S. A. Quantitative three-dimensional microstructure of a solid oxide fuel cell cathode. *Electrochem. Commun.*, 2009, **11**(5), 1052–1056.
 - 30 Wilson, J. R., Gameiro, M., Mischaikow, K., Kalies, W., Voorhees, P. W., and Barnett, S. A. Three-dimensional analysis of solid oxide fuel cell Ni-YSZ anode interconnectivity. *Microsc. Microanal.*, 2009, **15**, 71–77.
 - 31 Wilson, J. R., Kobsiriphat, W., Mendoza, R., Hiller, J. M., Chen, H.-Y., Miller, D. J., Thornton, K., Voorhees, P. W., Adler, S. B., and Barnett, S. A. Three-dimensional reconstruction of a solid-oxide fuel-cell anode. *Nature Mater.*, 2006, **5**, 541–544.
 - 32 Haughey, D. P. and Beveridge, G. S. G. Structural properties of packed beds – a review. *Canad. J. Chem. Eng.*, 1969, **47**, 130–140.
 - 33 Kim, I. C. and Torquato, S. Effective conductivity of suspensions of overlapping spheres. *J. Appl. Phys.*, 1992, **71**(6), 2727–2735.
 - 34 Rintoul, M. D. and Torquato, S. Computer simulations of dense hard-sphere systems. *J. Chem. Phys.*, 1996, **105**(20), 9258–9265.
 - 35 Torquato, S., Truskett, T. M., and Debenedetti, P. G. Is random close packing of spheres well defined? *Phys. Rev. Lett.*, 2000, **84**(10), 2064–2067.
 - 36 Truskett, T. M., Torquato, S., and Debenedetti, P. G. Towards a quantification of disorder in materials: distinguishing equilibrium and glassy sphere packings. *Phys. Rev. E*, 2000, **62**(1), 993–1000.

- 37 Rintoul, M. D. and Torquato, S. Reconstruction of the structure of dispersions. *J. Colloid Interface Sci.*, 1997, **186**, 467–476.
- 38 Asinari, P., Quaglia, M. C., von Spakovsky, M. R., and Kasula, B. V. Direct numerical calculation of the kinematic tortuosity of reactive mixture flow in the anode layer of solid oxide fuel cells by the lattice boltzmann method. *J. Power Sources*, 2007, **170**(2), 359–375.
- 39 Bentz, D. P. and Martys, N. S. Hydraulic radius and transport in reconstructed model three-dimensional porous media. *Transp. Porous Media*, 1994, **17**, 221–238.
- 40 Kenney, B., Valdmanis, M., Baker, C., Pharoah, J. G., and Karan, K. Computation of TPB length, surface area and pore size from numerical reconstruction of composite SOFC electrodes. *J. Power Sources*, 2009, **189**, 1051–1059.
- 41 Brosseau, C. Modelling and simulation of dielectric heterostructures: a physical survey from an historical perspective. *J. Phys. D, Appl. Phys.*, 2006, **39**, 1277–1294.
- 42 Torquato, S. *Random heterogeneous materials: microstructure and macroscopic properties*, 2002 (Springer-Verlag, New York).
- 43 Burganos, V. N. and Sotirchos, S. V. Diffusion in pore networks: effective medium theory and smooth field approximation. *AIChE J.*, 1987, **33**, 1678–1689.
- 44 Burganos, V. N. Monte Carlo simulation of gas diffusion in regular and randomized pore systems. *J. Chem. Phys.*, 1993, **98**, 2268–2278.
- 45 Burganos, V. N. Gas diffusion in random binary media. *J. Chem. Phys.*, 1998, **109**, 6772–6779.
- 46 Ioannidis, M. A., Kwiecien, M. J., and Chatzis, I. Electrical conductivity and percolation aspects of statistically homogeneous porous media. *Transp. Porous Media*, 1997, **29**, 61–83.
- 47 Mu, D., Liu, Z.-S., Huang, C., and Djilali, N. Prediction of the effective diffusion coefficient in random porous media using the finite element method. *J. Porous Mater.*, 2007, **14**, 49–54.
- 48 Sunde, S. Monte Carlo simulations of conductivity of composite electrodes for solid oxide fuel cells. *J. Electrochem. Soc.*, 1996, **143**, 1123–1132.
- 49 Torquato, S. and Kim, I. C. Efficient simulation technique to compute effective properties of heterogeneous media. *Appl. Phys. Lett.*, 1989, **55**(18), 1847–1849.
- 50 Zalc, J. M., Reyes, S. C., and Iglesia, E. The effects of diffusion mechanism and void structure on transport rates and tortuosity factors in complex porous structures. *Chem. Eng. Sci.*, 2004, **59**, 2947–2960.
- 51 Shikazono, N., Sakamoto, Y., Yamaguchi, Y., and Kasagi, N. Microstructure and polarization characteristics of anode supported tubular solid oxide fuel cell with co-precipitated and mechanically mixed Ni-YSZ anodes. *J. Power Sources*, 2009, **193**, 530–540.
- 52 Gommers, C. J., Bons, A.-J., Blacher, S., Dunsmuir, J. H., and Tsou, A. H. Practical methods for measuring the tortuosity of porous materials from binary or gray-tone tomographic reconstructions. *AIChE J.*, 2009, **55**(8), 2000–2012.
- 53 Izzo, J. R., Joshi, A. S., Grew, K. N., Chiu, W. K. S., Tkachuk, A., Wang, S. H., and Yun, W. Nondestructive reconstruction and analysis of SOFC anodes using X-ray computed tomography at sub-50 nm resolution. *J. Electrochem. Soc.*, 2008, **155**(5), B504–B508.
- 54 Einstein, A. *Investigations on the theory of the Brownian movement*, 1926 (Methuen, London, UK).
- 55 Golbert, J., Adjiman, C. S., and Brandon, N. P. Microstructural modeling of solid oxide fuel cell anodes. *Ind. Eng. Chem. Res.*, 2008, **47**, 7693–7699.
- 56 Schneider, L. C. R., Martin, C. L., Bultel, Y., Bouvard, D., and Siebert, E. Discrete modelling of the electrochemical performance of SOFC electrodes. *Electrochim. Acta*, 2006, **52**, 314–324.
- 57 Heinrich, J. C., Poirier, D. R., and Nagelhout, D. F. Mesh generation and flow calculations in highly contorted geometries. *Comput. Methods Appl. Mech. Eng.*, 1996, **133**, 79–92.
- 58 Tavakoli, R. CartGen: robust, efficient and easy to implement uniform/octree/embedded boundary Cartesian grid generator. *Int. J. Numer. Methods Fluid*, 2008, **57**, 1753–1770.
- 59 Cieslak, S., Ben Khelil S., Choquet, I., and Merlen, A. Cut cell strategy for 3-D blast waves numerical simulations. *Shock Waves*, 2001, **10**, 421–429.
- 60 Pattinson, J., Malan, A. G., and Meyer, J. P. A cut-cell non-conforming Cartesian mesh method for compressible and incompressible flow. *Int. J. Numer. Methods Eng.*, 2007, **72**, 1332–1354.
- 61 Sang, W. and Li, F. An unstructured/structured multi-layer hybrid grid method and its application. *Int. J. Numer. Methods Fluid*, 2007, **53**, 1107–1125.
- 62 OpenFOAM® (Open Field Operation and Manipulation). *The open source CFD toolbox. User guide version 1.6*, 2009 (OpenCFD Ltd, London, UK) available from <http://www.openfoam.com>.
- 63 Arpino, E., Carotenuto, A., Massarotti, N., and Nithiarasu, P. A robust model and numerical approach for solving solid oxide fuel cell (SOFC) problems. *Int. J. Numer. Methods Heat Fluid Flow*, 2008, **18**(7/8), 811–834.
- 64 Chan, S. H., Chen, X. J., and Khor, K. A. Cathode micro-model of solid oxide fuel cell. *J. Electrochem. Soc.*, 2004, **151**, A164–A172.
- 65 Chan, S. H. and Xia, Z. T. Anode micro model of solid oxide fuel cell. *J. Electrochem. Soc.*, 2001, **148**, A388–A394.
- 66 Chen, X. J., Chan, S. H., and Khor, K. A. Simulation of a composite cathode in solid oxide fuel cells. *Electrochim. Acta*, 2004, **49**, 1851–1861.
- 67 DeCaluwe, S. C., Zhu, H., Kee, R. J., and Jackson, G. S. Importance of anode microstructure in modeling solid oxide fuel cells. *J. Electrochem. Soc.*, 2008, **155**, B538–B546.
- 68 Ho, T. X., Kosinski, P., Hoffmann, A. C., and Vik, A., Numerical analysis of a planar anode-supported SOFC with composite electrodes. *I. J. Hydrog. Energy*, 2009, **34**, 3488–3499.
- 69 Jeon, D. H. A comprehensive CFD model of anode-supported solid oxide fuel cells. *Electrochim. Acta*, 2009, **54**, 2727–2736.
- 70 Joshi, A. S., Grew, K. N., Peracchio, A. A., and Chiu, W. K. S. Lattice Boltzmann modeling of 2D gas transport in a solid oxide fuel cell anode. *J. Power Sources*, 2007, **164**, 631–638.
- 71 Weller, H. G., Tabor, G., Jasak, H., and Fureby, C. A tensorial approach to computational continuum mechanics using object-oriented techniques. *Comput. Phys.*, 1998, **12**(6), 610–631.

- 72 **García-Camprubí, M., Sánchez-Insa, A., and Fueyo, N.** Multimodal mass transfer in solid-oxide fuel-cells. *Chem. Eng. Sci.*, 2010, **65**, 1668–1677.
- 73 **Mustata, R., Vali no, L., Barreras, F., Gil, M. I., and Lozano, A.** Study of the distribution of air flow in a proton exchange membrane fuel cell stack. *J. Power Sources*, 2009, **192**, 185–189.
- 74 **Siegel, C.** Review of computational heat and mass transfer modeling in polymer-electrolyte-membrane (PEM) fuel cells. *Energy*, 2008, **33**, 1331–1352.
- 75 **Drewry, H. P. G. and Seaton, N. A.** Continuum random walk simulations of diffusion and reaction in catalyst particles. *AIChE J.*, 1995, **41** (4), 880–893.
- 76 **Kim, I. C. and Torquato S.** Diffusion of finite-sized Brownian particles in porous media. *J. Chem. Phys.*, 1992, **96**(2), 1498–1503.
- 77 **Tomadakis, M. M. and Sotirchos, S. V.** Ordinary and transition regime diffusion in random fiber structures. *AIChE J.*, 1993, **39**, 397–412.
- 78 **Berson, A., Choi, H.-W., and Pharoah, J. G.** Determination of the effective gas diffusivity of a porous medium from the three-dimensional reconstruction of its microstructure: application to solid oxide fuel cells composite electrodes. *Phys. Rev. E.*, 2010, under review.
- 79 **Allen, T. T.** *Introduction to engineering statistics and six sigma: statistical quality control and design of experiments and systems*, 2006 (Springer, London).
- 80 **Weisstein, E. W.** Sphere–sphere intersection. From MathWorld-A Wolfram Web Resource, available from <http://mathworld.wolfram.com/Sphere-Sphere-Intersection.html>.
- 81 **Bouvard, D. and Lange, F. F.** Relation between percolation particle coordination in binary powder mixtures. *Acta Metall. Mater.*, 1991, **39**, 3083–3090.
- | | |
|---------------------------|---|
| elec | electron phase within porous media |
| f | 'face' of the control volume |
| \mathbf{f} | forcing vector |
| ion | ion phase within porous media |
| L | selected length of the computational domain (m) |
| n | exponent in Archie's power law or in percolation theory |
| pore | pore phase within porous media |
| \mathbf{q} | flux density of the phase |
| s | prescribed distance (m) |
| S | boundary surface area of the phase (m^2) |
| \mathbf{S}_f | outward-pointing face area vector |
| t | travel time (s) |
| V | volume of the phase (μm^3) |
| V_{solid} | volume of the solid contents,
$V_{\text{solid}} = V_{\text{elec}} + V_{\text{ion}}$ (μm^3) |
| V_{total} | volume of the sample domain,
$V_{\text{total}} = V_{\text{pore}} + V_{\text{elec}} + V_{\text{ion}}$ (μm^3) |
| α | bulk transport (or exchange) coefficient |
| α^{eff} | effective transport (or exchange) coefficient |
| $\partial\phi/\partial n$ | normal potential gradient |
| $\partial\Omega$ | surface boundary of the computational domain |
| $\Delta\phi$ | potential difference of the phase |
| ϵ | volume (or bond) fraction |
| ϵ_c | percolation threshold of the medium |
| ϵ_{phase} | volume fraction of each phase |
| κ | electrical (electron or ion) conductivity ($\text{kg m/s}^3 \text{K}$) |
| κ^{eff} | effective electronic or ionic conductivity ($\text{kg m/s}^3 \text{K}$) |
| λ | free path of gas molecules |
| $\langle\lambda\rangle$ | mean free path of gas molecules |
| $\langle\xi^2\rangle$ | mean-square displacement |
| σ | standard deviation |
| ϕ | relevant potential field |
| Φ | solution field of linear system |
| Ω | control volume of the computational domain |
| Ω_{phase} | arbitrarily phase region |

APPENDIX

Notation

\mathbf{A}	sparse linear matrix
d	diameter of the solid particle (μm)
$d\Omega$	differential volume
dS	differential surface
D	gas diffusivity for the pore phase (m^2/s)
D^{eff}	effective gas diffusivity (m^2/s)
eff	effective transport coefficient